This is the Pre-Published Version.

IEEE TRANSACTIONS ON INDUSTRIAL ELECTRONICS
The following publication Zhu, Z., Chen, L., Huang, P., Schönemann, L., Riemer, O., Yao, J., To, S., & Zhu, W.-L. (2020). Design and Control of a Piezoelectrically Actuated Fast Tool Servo for Diamond Turning of Microstructured Surfaces. IEEE Transactions on Industrial Electronics, 67(8), 6688–6697 is available at https://doi.org/10.1109/TIE.2019.2937051.

Design and control of a piezoelectrically actuated fast tool servo for diamond turning of micro-structured surfaces

Zhiwei Zhu, *IEEE Member*, Li Chen, Peng Huang, Lars Schönemann, Oltmann Riemer, Jianyong Yao, Suet To, *IEEE Member* and Wu-Le Zhu, *IEEE Member*

***Abstract*—This paper reports on the mechanism design, dimension optimization, closed-loop control, and practical application of a piezoelectrically actuated fast tool servo (FTS) for the diamond turning of micro-structured surfaces. With the mechanism, a finite element based analytical model is developed to theoretically relate the working performance with its structural dimensions. Considering its application for micro/nanocutting, the structural dimensions of the mechanism are deliberately determined through evolutionarily optimizing a comprehensive objective. To ultra-finely track the cutting trajectory with a high bandwidth, a PID controller together with the dynamics inversion based feedforward compensation is optimally designed with assistance of the Nyquist diagram, and a disturbance observer is further employed to compensate for the inherent hysteresis nonlinearity as well as external cutting force disturbances. Both open-loop and closed-loop experimental tests on the prototype suggest that a stroke of 15 μm and a closed-loop bandwidth of 1730 Hz are achieved. Taking advantage of the newly developed FTS, two typical micro-structured surfaces are ultra-precisely turned, well demonstrating the effectiveness of the FTS.**

***Index Terms*—Diamond turning, fast tool servo, compliant mechanism, disturbance observer, micro-structured surface.**

Manuscript received March 23, 2019; revised July 08, 2019; accepted August 09, 2019. This work was supported in part by the National Natural Science Foundation of China (51705254), and in part by the Natural Science Foundation of Jiangsu Province (BK20170836), the European Commission (EC)/ Research Grants Council (RGC) Collaboration Scheme (E-PolyU502/17), and the European Union's Horizon 2020 research and innovation program (767589). The author Z Zhu also thanks the financial support from Alexander von Humboldt-Stiftung, Germany.

Z. Zhu, L. Chen and J Yao are with School of Mechanical Engineering, Nanjing University of Science and Technology, Nanjing, 210094 JS, China (e-mail: zw.zhu@njust.edu.cn).

P. Huang is with College of Mechatronics and Control Engineering, Shenzhen University, Shenzhen, 518060 GD, China (e-mail: huangp@szu.edu.cn).

L. Schönemann and O. Riemer are with Leibniz Institute for Materials Engineering IWT, LFM, Bremen, and they are also with MAPEX Center for Materials and Processes, University of Bremen, 28359 Bremen, Germany (e-mail: riemer@iwt.uni-bremen.de).

S. To is with State Key Laboratory of Ultra-precision Machining Technology, Department of Industrial and Systems Engineering, The Hong Kong Polytechnic University, Kowloon, Hong Kong SAR, China (e-mail: sandy.to@polyu.edu.hk).

W.-L Zhu is with Department of Micro-Engineering, Kyoto University, Nishikyo-ku, 615-8540 Kyoto, Japan (corresponding author, e-mail: wule5033@gmail.com).

I. Introduction

FAST tool servo (FTS) was initially proposed to compensate for the motion errors of diamond turning machines [1], [2], and it was then widely extended to generate noncircular pistons [3], [4], non-axisymmetric freeforms [5], [6], and more complicated micro/nanostructured surfaces [7]–[9]. In general, a complete FTS mainly consists of three parts, namely the actuation, motion transmission, and motion control systems. To better serve for the industrial application, a variety of efforts have been devoted to improving performances of each system of FTS during the last three decades.

With respect to the generation of micro-structured surfaces, the position-varying shape with highly intensive features in the micron-scale commonly leads to a requirement for FTS to conduct oscillations with higher frequencies but shorter strokes when compared with the application for noncircular and freeform turning. To satisfy this requirement, the piezoelectric actuator (PEA) [3], [7], [10] and the Maxwell's normal stress electromagnetic force [11], [12] are introduced as two typical driving sources to achieve the high frequency oscillations, and the actuations are mainly supported and delivered through monolithic flexure mechanisms. Compared with the Maxwell's force, the commercially available PEA features much higher stiffness and much larger driving forces which are beneficial for diamond turning regarding the machining efficiency and machining stability [12], [13]. Therefore, the piezoelectrically actuated FTS will be more promising to oscillate the tool for the generation of micro-structured surfaces.

With respect to the flexure mechanism for FTS, the most direct design was to adopt a parallelogram mechanism having two parallel flexure linkages for translational motion guidance, and the PEA is arranged to actuate at the mid-point of the flexure linkage to have an one-stage motion amplification [3], [14]. Since the parasitic motion vertical to the main driving direction was not constrained for this configuration, the axisymmetry structure with double parallelogram mechanisms was then adopted in a more popular way to guide the tool [15]–[18]. With this design, taking advantage of the developed analytical model or finite element simulation, the multi-objective optimization was conducted to derive the optimal structural dimensions regarding the sufficient stroke, long fatigue life, high stiffness, and high working bandwidth [19]–[21]. However, as the PEA is directly connected with

© 2019 IEEE. Personal use of this material is permitted. Permission from IEEE must be obtained for all other uses, in any current or future media, including reprinting/republishing this material for advertising or promotional purposes, creating new collective works, for resale or redistribution to servers or lists, or reuse of any copyrighted component of this work in other works.

the end-effector holding the tool for this axisymmetry FTS, it is a little bit difficult to arrange the displacement sensor for motion capturing without affecting its working performance. Moreover, to expand the achievable stroke for FTS, more complex flexure mechanisms with multi-stage displacement amplifications were also deliberately designed. The large stroke as well as the low bandwidth induced by the relatively large moving inertia makes such FTS more suitable for the generation of freeforms with large sag values [6].

It is crucially important to establish a feedback control system for the piezoelectrically actuated FTS for ultra-fine tracking of the desired trajectory. With the piezo-electrically actuated mechanisms, a variety of linear and nonlinear controllers were developed mainly considering the hysteresis nonlinearity of PEAs [18], [22]–[25]. Generally speaking, all those methods could be directly applied for the trajectory tracking in FTS diamond turning. For example, the most basic proportional-integral-derivative (PID) type controller enhanced by the dynamics inversion based feedforwad compensation is commonly adopted to achieve better dynamic performances [15], [17]. In addition, the generalized fractional order PID based control system was also developed for FTS. However, more parameters to be tuned for the fractional order control systems may lead to an increased design complexity for practical application [26]. To gain high robustness regarding system uncertainty, the sliding mode based control strategies were developed for FTS in the academic society [3], [16], [18], [27]. With the those controllers, the first-order dynamics of the power amplifier is commonly ignored during the design to avoid over-large noises induced by the third order derivative of the practical motion. The insufficient consideration of system dynamics will inevitably lead to a poor tracking capability especially for high frequency applications. Moreover, it is also very challenging to eliminate the chatter for the sliding mode based control systems [28], and the system uncertainties are treated as disturbances rejected through system robustness, which increases the control burden for trajectory tracking.

Be different from the piezo-electrically actuated nanopositioning stages, FTS features quasi-periodic trajectory as well as time-varying disturbances including cutting forces and system vibrations. Considering the quasi-periodic trajectory, the internal model based controllers are particularly designed to ultra-finely track the trajectory with specified periodic components. The plug-in repetitive controller [14], [29] and the adaptive feedforward cancellation controller [6] are two typical ones developed from the internal model principle. With the internal model based control, a main controller, for example, the PID-type [14], [29] or phase shaping controller [11], is commonly employed to tune the system dynamics. Compared with the repetitive controller, the adaptive feedforward cancellation is more promising as it is much easier to be implemented to process signals with multiple frequencies as well as to compensate for system phase variations [30]. Although extremely high tracking accuracy can be achieved by implementing the internal model based control, the periodicity for the controller design must be strictly consistent with that of the trajectory or disturbances, suggesting that the controller must be changed with respect to surface shapes and cutting parameters. Furthermore, considering the external disturbances, the active disturbance rejection control is proposed for the electromagnetic force driven FTS featuring high linearity, which adopts an extended state observer to estimate and compensate for the generalized disturbances [4], [31]. Generally speaking, the active disturbance rejection control is promising considering its strong capability to reject external disturbances. However, the nonlinear frame imposes challenge for tuning the control parameters on basis of the classic control theory, and there is also a limited consideration of parameterizable uncertainties of the system [31], [32].

In this paper, a piezoelectrically actuated FTS is developed and comprehensively demonstrated. With this FTS, a novel mechanical structure is proposed by fully considering the elimination of parasitic motions, the difficulty for sensor arrangement, and the conflict between motion amplification and system bandwidth. Dimensions of the FTS are then evolutionarily optimized to achieve the kinematic and dynamic targets. To simplify the control system for saving the computation time, a linear control strategy is newly developed by essentially addressing the two featuring issues related to piezo-electrically actuated FTSs, namely the system nonlinearity and external disturbance. Finally, the performance of the developed FTS is demonstrated through practically turning a sinusoidal micro-grid surface and a typical micro-lens array.

II. Design of The Fast Tool Servo

A. Mechanical design and optimization of the FTS

The three-dimensional (3-D) model of the assembled FTS is shown in Fig. 1 (a), and the main flexural part is illustrated in Fig. 1 (b). The end-effector is supported by the well-known double parallelogram mechanism for parasitic motion constraint, and each linkage for the double parallelogram mechanism consists of two right circular flexure hinges connected by one flexure beam. The input-end of the mechanism is guided by one parallelogram mechanism using the leaf-spring flexure hinge. It is noteworthy that the two parallelogram mechanisms are especially designed to be unsymmetrical to reduce the overall size as well as to decrease the moving mass for improving its natural frequency.

During working, the PEA is actuated at the middle point of one flexure linkage, and this unique configuration may lead to outperforming features as:

1) an amplification of the input actuation motion through the equivalent lever-amplifier mechanism;
2) a sufficient space for the capacitive sensor to conveniently capture the displacement most directly related to the diamond tool.

To describe the elastic deformation behavior of the compliant mechanism, the finite element based analytical model as introduced in Ref. [33], [34] is adopted, and the corresponding nodes and elements of the mechanism for the finite element based analytical model is marked in Fig. 1 (b). Overall, the mechanism consists of 18 elements which are denoted from number 1 to 18 in Fig. 1 (b), and the input and output ports of the mechanism are denoted by node ⑱ and node ④, respectively. Following the Newton's second law, the

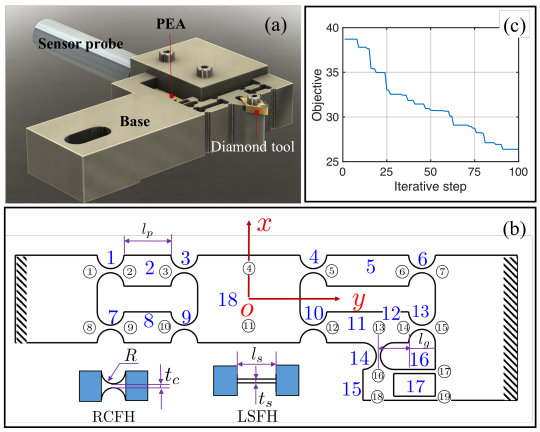

Fig. 1. Schematic of the piezoelectrically actuated FTS, (a) the 3-D assembled model, (b) the mechanical structure of the main flexural part with equivalent nodes and elements, and (c) the convergence for the evolutionary optimization.

governing equation for the elastic motion of each node can be expressed in the global coordinate system $o-xy$ as

$$\mathbf{M}\ddot{\mathbf{x}} + \mathbf{K}\mathbf{x} = \mathbf{F} \tag{1}$$

with

$$\begin{cases} \mathbf{F} = [\mathbf{F}_1, \cdots, \mathbf{F}_n, \cdots, \mathbf{F}_{19}]^{\mathrm{T}} \\ \delta = [\delta_1, \cdots, \delta_n, \cdots, \delta_{19}]^{\mathrm{T}} \end{cases} \tag{2}$$

where n denotes the node number, and $\mathbf{K}$ and $\mathbf{M}$ are the equivalent stiffness and mass matrix of the mechanism which can be constructed according to the algorithm presented in Ref. [33]. $\mathbf{F}_n = [F_{x,n},\ F_{y,n},\ M_{z,n}]$ and $\delta_n = [\delta_{x,n},\ \delta_{y,n},\ \theta_{z,n}]$ are the planar force and displacement on the n-th node.

Considering the fact that the node ①, ⑦, ⑧, ⑮, ⑰, and ⑲ are grounded, the corresponding elements in the columns and rows in Eq. 1 are removed as they have no motions. By means of applying a unit force vector $\mathbf{F}_{18} = [1, 0, 1 \times l_{18}]$ on node ⑱ with l_{18} denoting the y-axial distance from this node to the ox axis, the resulting x-axial displacement of this node can be calculated by solving Eq. 1. Hence, the input stiffness k_{in} along the actuation direction can be obtained according to its definition as $k_{in} = |\delta_{x,18}|^{-1}$. Similarly, by separately applying a unit force vector $\mathbf{F}_4 = [1, 0, 0]$ on the output node ④, the output stiffness along the actuation direction can be determined using the resulting deformation $\delta_{x,4}$ by $k_{ot} = |\delta_{x,4}|^{-1}$. In addition, from the relationship in Eq. 1, the first natural frequency f_o of the system can be obtained as the minimum values of $\hat{f}_i$ satisfying $\left|\mathbf{K} - (2\pi\hat{f}_i)^2\mathbf{M}\right| = 0$.

With respect to a FTS, the stroke and natural frequency are two basic factors reflecting its working performance [35]. Moreover, a sufficient output stiffness is essentially required to guarantee the turning stability [35], [36]. Taking advantage of the theoretically derived input stiffness k_{in}, amplification ratio A_r, natural frequency f_o, and output stiffness k_{ot}, the multiple design objectives are weighted to be a mono-objective optimization problem with the objective function being defined by

$$\min O = \omega_1 \left| \frac{k_p d_o A_r}{k_p + k_{in}} - \hat{s}_o \right| + \omega_2 \left| k_{ot} - \hat{k}_{ot} \right| + \omega_3 \left| f_o - \hat{f}_o \right| \tag{3}$$

where the first term in the right side is the stroke for the mechanism, $k_p = 100$ N/μm and $d_o = 15$ μm are the stiffness and nominal stroke of the PEA, respectively; $\omega_1 = 2.8$, $\omega_2 = 1$ and $\omega_3 = 2$ are the weights for the objectives. Considering bandwidth of the power amplifier and nominal stroke of the PEA, the desired stroke and natural frequency are set as $\hat{s}_o$=30 μm and $\hat{f}_o$=3.5 kHz, respectively. Since the normal cutting force in diamond turning of micro-structured surfaces is in the range of dozens or hundreds of millinewtons [37], [38], the desired output stiffness is set as $\hat{k}_{ot} = 10$ N/μm to resist the cutting forces.

TABLE I
OPTIMIZED STRUCTURAL PARAMETERS.

R mm	l_s mm	l_p mm	t_c mm	t_s mm	α
1.3	4.6	8	0.4	0.4	0.37

The material for the design is spring steel with elastic modulus, Poisson's ratio, and mass density of 206 GPa, 0.26, and 7.86 $\times 10^3$ kg/m^3, respectively. Considering dimensions of the two types of flexure hinges and the relative positions between these hinges as marked in Fig. 1 (b), there are totally six structural dimensions to be determined, and an indirect parameter $\alpha = \frac{l_g}{l_p}$ is defined to obtain l_g from l_p. Therefore, a nonlinear optimization problem with multiple variables is constructed for the FTS. Herein, an improved differential algorithm is conducted for solving this problem, and the convergent path for the optimization is shown in Fig. 1 (c). After optimization, the obtained structural parameters and the corresponding performances of the optimized mechanism are presented in Table I and Table II, respectively.

B. Finite element verification

To verify the analytically optimized structure, finite element analysis (FEA) using the commercial software ANSYS/Workbench modulus is conducted, and the mechanical structure is meshed by the 3D tetrahedron element. Through applying a force of 100 N on the input-end along the actuation direction, the resulting static deformation of the mechanism is illustrated in Fig. 2 (a). By means of the modal analysis in FEA, the first mode shape is also obtained as shown in Fig. 2 (b) with a natural frequency of 3321 Hz. The second order natural frequency is simulated to be 17 kHz which is much higher than the first natural frequency, suggesting that it is beneficial for the FTS to maintain the desired dynamics during turning. The FEA result is comparatively summarized in Table II with that obtained by analytical model, and a good agreement between them demonstrates the effectiveness of the optimization as conducted.

One feature of FTS turning is its high frequency oscillation which leads the potential fatigue issue to be carefully addressed during the design [35], [39]. Herein, the modified Goodman approach using the equivalent stress is employed to

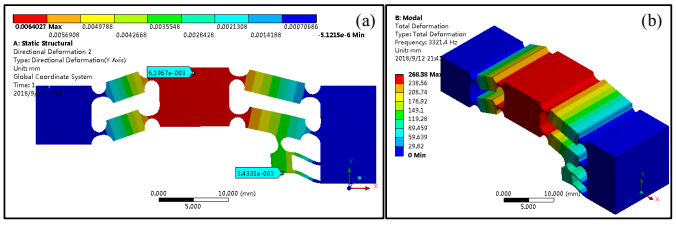

Fig. 2. Schematic of the piezo-actuated flexure mechanism, (a) the 3-D assembled model, and (b) the mechanical structure of the actuation part with equivalent nodes and elements.

evaluate the safety factor S_f of the optimized mechanism for its fatigue life characterization. Under the static loading with a maximum input displacement of 15 μm, the maximum stress is simulated to be σ_m =340 MPa through FEA.

To investigate the fatigue behavior, the stress is assumed to be harmonically varied between 0 and σ_m. Considering the fatigue stress concentration factor $K_f = 1.4$, ultimate strength $\sigma_u = 1274$ MPa, and endurance limit σ_e=700 MPa for the steel [39], the safety factor S_f is determined by [21]

$$S_f = \left(\frac{K_f \sigma_m}{2\sigma_e} + \frac{K_f \sigma_m}{2\sigma_u} \right)^{-1} \tag{4}$$

which leads to $S_f \approx 1.9 > 1$, demonstrating an infinite fatigue life of the optimized mechanism [21].

Note: The optimized result exhibits a good comprehensive working performance, and it is acceptable to perform a high quality diamond turning for the generation of micro-structured surfaces. More practically, if necessary, different balances between those conflict design targets can be realized to achieve any specified working performances through tuning the target weights in Eq. 3.

TABLE II
PERFORMANCES OF THE OPTIMIZED STRUCTURE.

	k_{in} N/μm	k_{out} N/μm	f_o Hz	A_r
Anal.	28.32	4.63	2949	1.91
FEA	29.12	6.06	3321	1.81
Error	3.06%	23.60%	11.20%	5.52%

III. CONTROL SYSTEM DESIGN FOR THE FTS

Although the hysteresis is widely compensated for piezoelectrically actuated nanopositioning stages, less attention was paid on that of the piezoelectrically actuated FTS [40]. Currently, the inverse hysteresis model based feedforward compensation is the most popular way to deal with the hysteresis, and it requires high accurate modeling and identification of the complex hysteresis. However, the state-of-the-art hysteresis models are still insufficient to describe this nonlinear behavior covering a wide frequency spectrum. Inspired by the work in Ref. [41], [42], the linear nominal model based DOB is employed to compensate for the hysteresis through treating it as an external disturbance imposed on the linear system.

A. Dynamics modeling of the FTS

Considering the coupled effect between the mechanical structure and actuation system, the electromechanical dynamics model of the FTS is constructed to facilitate the design of its control system. Considering the amplification of the mechanism, the dynamics equation for the input end can be expressed by

$$m\ddot{x}_{in}(t) + c\dot{x}_{in}(t) + k_{in}x_{in}(t) = F_p \tag{5}$$

where m and c are the equivalent moving mass and damping coefficient, respectively; and F_p is the driving force generated by the PEA.

Considering the hysteresis of the PEA, the relationship between the input voltage and actuation force is decomposed into a linear term and a nonlinear hysteresis term, namely

$$F_p = k_p \Lambda u_{in}(t) + \hbar(t) \tag{6}$$

where $\hbar(t)$ denotes the nonlinear hysteresis force which can be modeled through any differential or operator based hysteresis models, and Λ is the equivalent piezoelectric coefficient. In general, the nonlinear hysteresis is demonstrated to be bounded, that is $|\hbar(t)| \leq \hbar_m := \sup |\hbar(t)|$ [41].

By approximating the PEA as an equivalent capacitance C_p with a resistance R_p, the relationship between the command voltage $u(t)$ and the driving one $u_{in}(t)$ amplified by the power amplifier can be expressed by

$$R_a \left[C_p \dot{u}_{in}(t) + \frac{u_{in}(t)}{R_p} \right] + u_{in}(t) = K_a u(t) \tag{7}$$

where R_a and K_a are the equivalent resistance and amplification gain of the power amplifier, respectively.

Since the second natural frequency is much higher than the first one for the FTS, the output motion of the end-effector can be obtained as $y(t) = A_r x_{in}(t)$ for a wide range of the working frequency. Through setting the bounded hysteresis force as an external disturbance, the nominal transfer function relating the end-effector motion and command voltage can be linearly expressed by

$$P_m(s) = \frac{Y(s)}{U(s)} = \frac{\epsilon \omega_0^2}{(1+\tau s)\left(s^2 + 2\xi_0 \omega_0 s + \omega_0^2\right)} \tag{8}$$

where $Y(s) = A_r X_{in}(s)$, $\omega_0 = \sqrt{\frac{k_{in}}{m}}$, $\xi_0 = \sqrt{\frac{c^2}{4mk_{in}}}$, $\tau = \frac{R_a R_p C_p}{R_a + R_p}$, and $\epsilon = \frac{k_p \lambda K_a R_p A_r}{(R_a + R_p) k_{in}}$.

B. Model based controller design

The control system for the FTS is illustrated in Fig. 3, Besides the DOB, a typical PID controller with a dynamics inversion based feedforward compensator is adopted for the trajectory tracking. Since the DOB is to compensate for the lumped disturbance imposed on the control system, the hysteresis as well as the practical external disturbance from the cutting process (i.e., cutting forces, machine vibrations, etc.) can be compensated by the DOB. Considering that only the cut-off frequency is to be tuned for the DOB, the proposed control system is very convenient to be implemented for engineering applications.

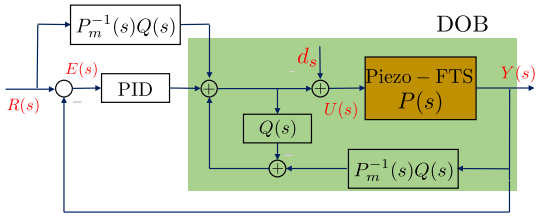

Fig. 3. Schematic of the closed-loop system for the FTS.

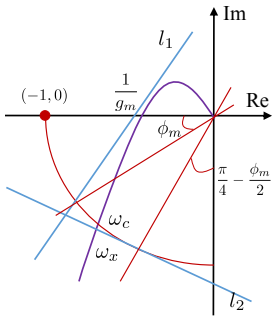

Fig. 4. Schematic of the Nyquist diagram of the open-loop system.

1) Optimized PID control: The gain margin, phase margin and crossover frequency of the open-loop transfer function are the key performances for a control system from the viewpoint of frequency domain analysis. Considering the sampling rate Ω, the adopted PID can be expressed by

$$C(s) = \rho_1 + \frac{\rho_2}{s} + \rho_3 \frac{\Omega s}{s+\Omega} \tag{9}$$

where ρ_1, ρ_2, and ρ_3 denote the proportional, integral, and derivative gain for the PID controller, respectively.

In the Nyquist diagram, a given gain and phase margin can determine a line as marked by l_1 in Fig. 4(a). Considering another line l_2 which is tangent to the unit circle at a point with a phase angle being of $\gamma = \frac{\pi}{4} - \frac{\phi_m}{2}$, the angular frequency ω_x which is at the intersecting point between the unit circle and the line l_2 separates the crossover frequency to be above the line l_2, namely $\omega_c \geq \omega_x$. Therefore, assurance of the specified gain and phase margin as well as the crossover frequency can be transform to be the following geometry constraints [43]:

1) To assure the gain and phase margin, the Nyquist curve of the open-loop system $G(s) = C(s)P_m(s)$ should be at the right side of the line l_1.
2) To keep the crossover frequency be greater than the given ω_x, the Nyquist curve of the open-loop system $G(s)$ should be below the line l_1 and above the line l_2.

In this paper, the main design goal for the PID controller is to maximize the low-frequency gain (i.e., the integration gain) of the system to reject the low-frequency disturbance and to minimize the steady error [43]. Assume the points on lines l_i $(i = 1, 2)$ can be expressed by $f(x + iy, l_i) = 0$, the specified performance can be mathematically described as a constrained optimization problem by [43]:

$$\max \rho_2 \tag{10}$$

subject to

$$\begin{aligned} &f\left(C_L(j\omega)P_m(j\omega), l_1\right) < 0 \text{ for } \omega > \omega_x \\ &f\left(C_L(j\omega)P_m(j\omega), l_2\right) > 0 \text{ for } \omega > \omega_x \\ &f\left(C_L(j\omega)P_m(j\omega), l_2\right) < 0 \text{ for } \omega \leq \omega_x \end{aligned} \tag{11}$$

In this study, the required gain and phase margin for the optimization are set as $g_m = 1.5$ and $\phi_m = 50\,\text{deg}$ for defining the line l_1, and the crossover frequency is set as $\omega_c = 1000\pi$ rad. The linear constrained problem in Eq. (10) can be easily solved by means of the simple linear programming optimization through MATLAB.

2) Disturbance observer: The DOB structure is presented in the highlightened block in Fig. 3, and P_m^{-1} denotes the inversion of the nominal model for the FTS. The key for the employment of a DOB is to design a low pass filter $Q(s)$, which is used to make the transfer function $P_m^{-1}(s)Q(s)$ proper as well as to guarantee the stability of the control system [41], [44]. Considering the relative degree of the system nominal model in Eq. 8, a third order Butterworth low-pass filter is employed, which can be expressed by

$$Q(s) = \frac{N_q(s, \tau_{qc})}{D_q(s, \tau_{qc})} = \frac{1}{(\tau_{qc}s + 1)\left[(\tau_{qc}s)^2 + \tau_{qc}s + 1\right]} \tag{12}$$

where $\tau_{qc} = \frac{2\pi}{\omega_{qc}}$ with $\omega_{qc} > 0$ being the cut-off frequency of the filter.

With assistance of the DOB, the system output $Y(s)$ subjecting to a disturbance $d_s(s)$ can be obtained as

$$Y(s) = \frac{(1 - Q(s))\left(P_m(s) + \mathcal{H}(s)\right)}{1 + P_m^{-1}(s)Q(s)} d_s(s) \tag{13}$$

where $\mathcal{H}(s)$ denotes the modeling uncertainty, and $P(s) = P_m(s) + \mathcal{H}(s)$ represents the practical model for the FTS.

Considering that $Q(j\omega) \approx 1$ in the low frequency range for the filter, the resulting output in terms of the lumped disturbance and model uncertainties can be approximately rejected for working in the low frequency range [45].

3) Feedforward compensation: Since the system hysteresis nonlinearity is treated as the model uncertainty to be compensated by the DOB, only a dynamics inversion based linear feedforward compensator is adopted to improve the dynamics response of the control system.

Accordingly, the compensator can be simply defined as

$$F_c(s) = P_m^{-1}(s)Q_c(s) = P_m^{-1}(s)\frac{N_q(s, \tau_f)}{D_q(s, \tau_f)} \tag{14}$$

where $Q_c(s) := Q(s, \tau_f)$ is a third-order Butterworth low-pass filter defined in Eq. 12 with a cut-off frequency of $\omega_f = \frac{2\pi}{\tau_f}$.

C. System stability

Since the feedforwad compensator does not change the stability of the closed-loop system, we only focus on the stability of the control system consisting of the PID and DOB controllers. Considering the physical property of the piezoelectrically actuated compliant mechanism, the plant model $P(s)$ can be assumed to belong to a set of transfer functions $\mathcal{P}(s)$ for which all the coefficients of its numerator and denominator are positive. Taking advantage of this assumption, the robust internal stability of the control system can be demonstrated following the work done in Ref. [41], [45], [46]:

Proposition 1: There is an upper boundary $\hat{\tau}_s > 0$, for all $\tau_{qc} \in (0, \hat{\tau}_s)$ in Eq. 12, the closed-loop system is robustly internally stable if the following three conditions are satisfied:

1) the closed loop system $G(s)$ using only the PID controller is stable, where $G(s)$ is:

$$G(s) = \frac{C(s)P_m(s)}{1 + C(s)P_m(s)} \tag{15}$$

2) the plant $P(s)$ is minimum phase and stable;
3) $P_f(s)$ is Hurwitz, where

$$P_f(s) := D_q(s,1) + \left(\lim_{s\to\infty} \frac{P(s)}{P_m(s)} - 1 \right) N_q(s,1) \tag{16}$$

To check the stability of the control system, the first condition in Proposition 1 is quite natural, and it can be easily guaranteed during the design of the PID controller with respect to the identified nominal model $P_m(s)$. In common, it is obviously true that the piezoelectrically actuated compliant mechanism with high first mode gain is minimum phase and stable [41].

Considering the fact that the mechanism for the FTS works in the small elastic deformation region and the hysteresis nonlinearity is usually less than 20% of the full motion span, the following relationship can be obtained:

$$R_d := \lim_{s\to\infty} \frac{P(s)}{P_m(s)} - 1 = \lim_{s\to\infty} \frac{\mathcal{H}(s)}{P_m(s)} \in (-1, 1) \tag{17}$$

Recall the employed third-order Butterworth filter in Eq. 12, the term $P_f(s)$ can be expressed as

$$P_f(s) = s^3 + 2s^2 + 2s + (1 + R_d) \tag{18}$$

Obviously, $P_f(s)$ is Hurwitz and the control system is of robust internal stability when a stable PID control system is designed. It is noteworthy that the third condition can be always guaranteed by adopting a proper filter, even for the system subjecting to arbitrarily large uncertainties [46].

IV. Experimental Testing

A prototype using spring steel is produced using the optimized structural dimensions. During testing, the FTS is installed on a three-axial ultra-precision machine tool (Moore Nanotech 450 UPL, USA) which is also used to conduct the practical turning experiments as described in the following section. The experimental setup is shown in Fig. 5.

To construct the FTS, a PEA with a nominal stroke of 15 μm is employed (PI P-887.51, Germany) together with a corresponding power amplifier having a gain of 10 ± 0.1 (PI E617.001, Germany). The generated motion at the output end is captured through a capacitive displacement sensor (Microsense 5810 module with probe 5503, USA) with the measurement range and bandwidth of 500 μm and 20 kHz, respectively. A data acquisition board (NI PCI-6259, USA) is adopted for the transfer and collection of the output command and input displacement, respectively. With the feedback control, the Matlab/Simulink module in the Desktop Real-Time environment is constructed to practically perform the designed control algorithm.

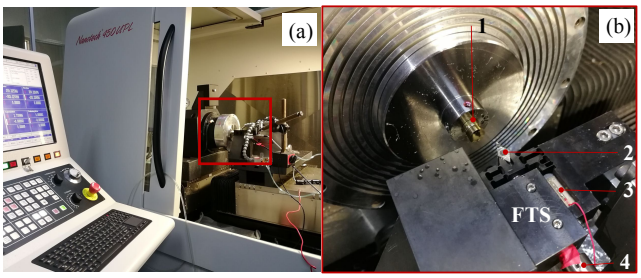

Fig. 5. Experimental setup of the FTS, (a) the ultra-precision machine tool with the installed FTS, and (b) an enlarged view of the FTS, where 1: the workpiece installed on the spindle, 2: diamond tool, 3: piezoelectric actuator, 4: capacitive sensor probe.

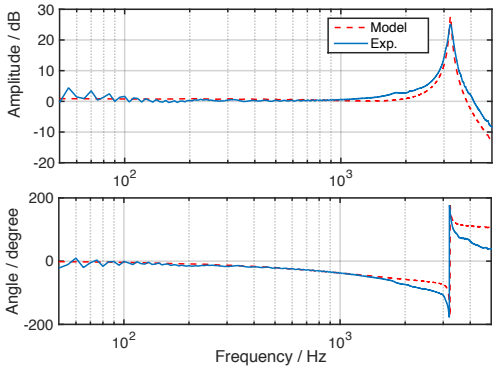

Fig. 6. Characteristics of the frequency response function for the FTS.

A. The open-loop performance

By adopting a harmonic voltage from 0 to 10 V, the practical stroke is measured to be around 18 μm. To identify the system dynamics in Eq. (8), the frequency domain characteristic of the FTS is measured through sweep excitation in the open-loop mode. During the sweep excitation, the voltage amplitude of the sweep command is 1 V, and the frequency linearly varies from 10 Hz to 5 kHz.

Through fast Fourier transform of the sweep command and the corresponding response, the resulting frequency response function is calculated and further illustrated in Fig. 6. From the amplitude-frequency response in Fig. 6, the first natural frequency can be identified as $\omega_0 = 2\pi f_o$ with $f_0 = 3215$ Hz which shows a good accordance with the designed value (3321 Hz as obtained by FEA). Through tuning the resonant peak and the phase changes, the system parameters in Eq. (8) are identified to be $\xi = 0.008$, $\tau_s = 1.5 \times 10^{-4}$, and $\epsilon = 1.1013$. Therefore, the identified nominal model for the FTS can be obtained as

$$P_m(s) = \frac{4.5 \times 10^8}{(1 + 1.5 \times 10^{-4} s)\,(s^2 + 323.2s + 4.08 \times 10^8)} \tag{19}$$

The resulting frequency response function for the identified model in Eq. (19) is comparatively presented in Fig. 6. Overall, the theoretical response matches well with the practically measured one, suggesting that the identified nominal model of the FTS is reliable for the controller design.

B. The closed-loop performance

To construct the control system, the cut-off frequencies of the filters for the DOB and feedforward compensator are set as 800 Hz and 2 kHz, respectively. With assistance of the identified model, the PID controller is optimized to be:

$$C(s) = \frac{0.28(s^2 - 3.4 \times 10^4 s + 5.3 \times 10^8)}{s(s + 5 \times 10^4)} \tag{20}$$

To investigate the trajectory tracking capability of the FTS, a harmonic signal with a frequency of 100 Hz and an amplitude of 5 μm is employed as the desired motion. The tracking performances of the control system using three controllers including the PID, PID with feedforward compensator (denoted as PID+FC), and PID with feedforward compensator and DOB (denoted as PID+FC+DOB), are comparatively studied, and the tracking results for all the three conditions are illustrated in Fig. 7 (a), and the corresponding tracking errors are further presented in Fig. 7 (b).

As shown in Fig. 7 (b), the maximum tracking error for the control system only using PID is about ± 0.85 μm, and it is then reduced to be about ± 0.35 μm by conducting the feedforward compensation. Tacking advantage of the DOB, the tracking error for the designed control system (PID+FC+DOB) is further decreased to be about ± 0.18 μm which is only about $\pm 1.5\%$ of the desired motion, showing an improvement of about 78.8% and 48.6% when compared with the control systems using only PID and PID with feedforward compensator, respectively. Overall, the result as obtained demonstrates the necessary and effectiveness of embedding the designed feedforward compensator and DOB for the basic PID control system.

With respect to a recently reported FTS in Ref. [18], an adaptive terminal sliding mode controller was deliberately designed for a similar piezo-electrically actuated FTS having a stroke less than 10 μm and natural frequency around 6 kHz. The following error was reported to be $\pm 2.5\%$ for tracking a harmonic motion with a frequency of 100 Hz. The relative error is slightly higher than that obtained in this study. Considering the fact that higher natural frequency may lead to better dynamic tracking accuracy using the same control strategy, the result well suggests the superiority of the proposed control system by combining PID, feedforward compensator and DOB.

To give a comprehensive evaluation of the dynamics of the closed-loop FTS system, a sweep command with the frequency ranging from 0 to 2 kHz is adopted to excite the closed-loop system (PID+FC+DOB). Similarly, the resulting frequency response function is calculated and illustrated in Fig. 8. Overall, the amplitude frequency function exhibits a relatively flat feature before 100 Hz. It will commonly lead to a relatively small tracking error within this frequency range which also shows a good accordance with the error observed in the time domain in Fig. 7. Moreover, as shown in Fig. 8, the working bandwidth of the FTS system is found to be 1730 Hz where an amplitude attenuation of -3 dB occurs.

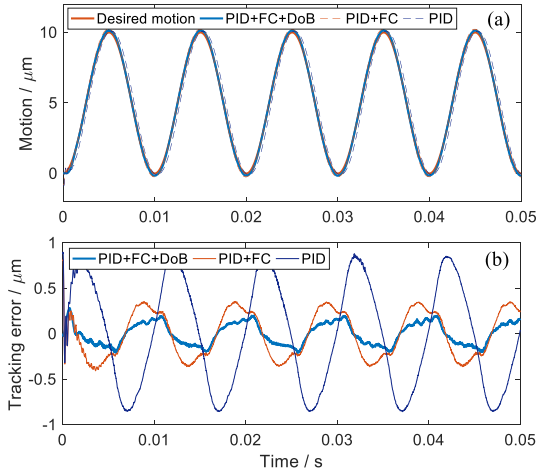

Fig. 7. Tracking performance of the FTS without cutting, (a) the desired and practical motions, and (b) the tracking errors.

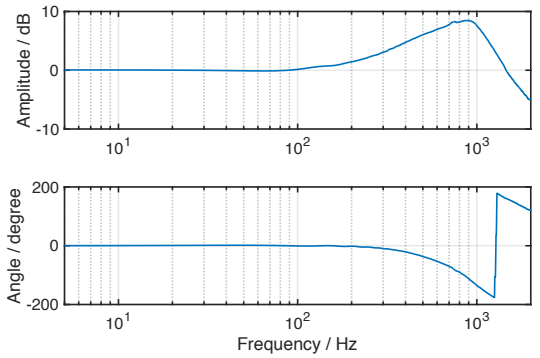

Fig. 8. The frequency response function of the close-loop system.

V. FTS Turning of Micro-structured Surfaces

To demonstrate the effectiveness of the constructed FTS system, the practical turning of two typical micro-structured surfaces are conducted based on the mentioned ultra-precision machine tool as illustrated in Fig. 5. Considering the high intensity of the surface micro-structures, the spindle rotates with a constant speed of 15 rpm, and the x-axial slide concurrently moves with a constant velocity of 5 μm/rev. To generate the micro-structured surface, the FTS which is fixed on the x-axial slide of the machine tool will precisely actuate the diamond tool to follow the desired toolpath which is deliberately determined based on the shapes of both the diamond tool and desired surface.

Herein, a round edge natural single crystal diamond tool (Contour Fine Tooling, UK) is employed with zero rake angle, and the nose radius and clearance angle are 0.1 mm and 7°, respectively. First of all, a harmonic micro-grid surface which can be mathematically expressed in its local coordinate system by $z = S(x, y) = A_s \cos(2\pi f_s x) + A_s \sin(2\pi f_s y)$ is turned using the FTS. The amplitude and spatial frequency for the surface are $A_s = 1.25$ μm and $f_s = 5$, respectively.

After turning, the generated surface is measured through a white light interferometer based optical surface profiler (Bruker ContourGT-X8, USA). The 3-D micro-topography of

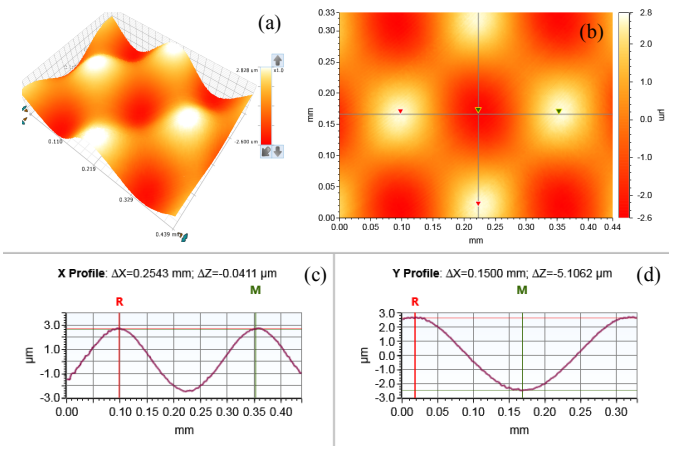

Fig. 9. Characteristics of the generated micro-grid surface, (a) the 3-D micro-topography, (b) the projected 2-D view, and the cross-sectional profile along the (c) horizontal and (d) vertical directions.

the resulting machined surface is illustrated in Fig. 9 (a), and the projected 2-D view is further shown in Fig. 9 (b) featuring uniformly distributed contours. The cross-sectional profiles along the horizontal and vertical directions as marked in Fig. 9 (b) are further given in Figs. 9 (c) and (d), respectively. As shown in Figs. 9 (c) and (d), the practically generated spatial periodicity and structural height are measured to be 254.3 μm (ΔX) and 5.1 μm (ΔZ), respectively. The practically obtained dimensional feature exhibits a good accordance with the desired micro-grid surface which has a periodicity of 250 μm and a height of 5 μm, respectively.

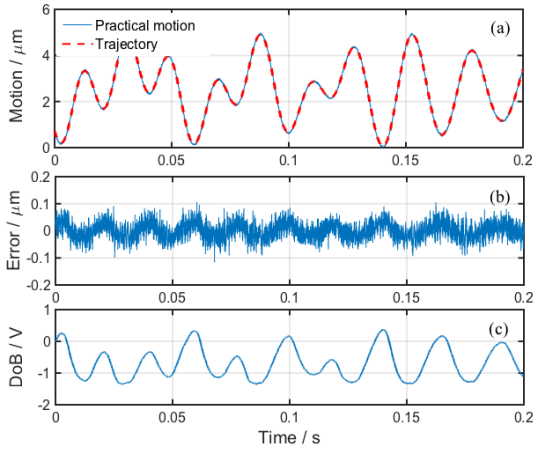

Fig. 10. Tracking performance of the FTS in turning the harmonic micro-grid surface, (a) the practical and desired tool motion, (b) the tracking error, and (c) the output of the DOB.

Considering the cutting force as the external disturbance, the practical tracking performance in turning the micro-structured surface is further illustrated in Fig. 10 (a), and a good agreement between the desired and practical motion is observed, irrespective to the disturbance. The tracking error and estimated voltage from the DOB are further shown in Figs. 10 (b) and (c), respectively. The voltage from DOB ranges from -1.3 V to 0.35 V which is jointly caused by the external disturbance and system hysteresis. Furthermore, the maximum error is observed to be within ± 0.07 μm during turning which is about $\pm 1.4\%$ of the full motion range, demonstrating that the control system is capable to conduct high accuracy trajectory tracking under practical turning.

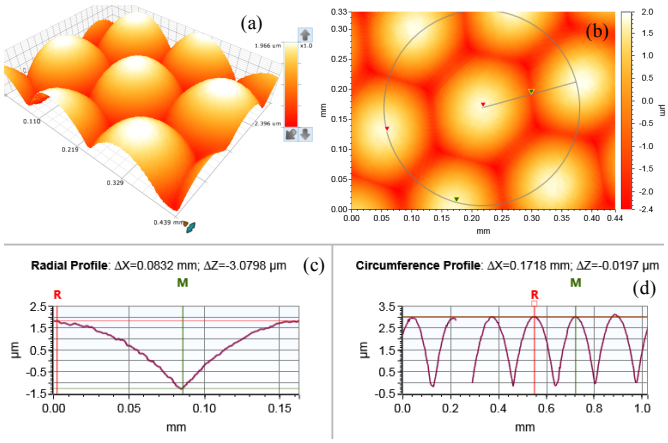

Fig. 11. Characteristics of the generated micro-lens array, (a) the 3-D micro-topography, (b) the projected 2-D view, and the cross-sectional profile along the (c) horizontal and (d) vertical directions.

As another demonstration, a typical hexagonal spherical micro-lens array is generated with the radius and height of each lenslet being designed as 0.2 mm and 4 μm, respectively. The same cutting parameters as that used for the micro-grid surface are employed. Similarly, the resulting concave micro-lens array and its corresponding 2-D projected view are captured through the optical surface profiler and illustrated in Figs. 11 (a) and (b), respectively. The radial cross-sectional profile in Fig. 11 (c) shows that the relative distance between centers of any two successive lenslets is about 171.8 μm, and the maximum height difference along the circumference direction is about 3.08 μm as shown in Fig. 11 (d). For the hexagonal structure, the theoretical relative distance and structure height can be calculated to be 173.2 μm and 3 μm, respectively. Overall, the relatively small deviation between the practical and desired profiles further demonstrates the effectiveness of the designed FTS for diamond turning.

VI. Conclusion

In this paper, a piezoelectrically actuated fast tool servo (FTS) is developed for the diamond turning of micro-structured surfaces. With the FTS, a novel compliant mechanism with one-stage amplification is designed for the support and motion guidance of the diamond tool. With full consideration of the purpose for micro/nanocutting, the multi-objective optimization of the structural dimensions is conducted for the mechanism, followed by further verification through the finite element analysis from both static and dynamic aspects.

On basis of the identified system dynamics, a feedback control strategy is developed for the FTS for which a PID controller is primarily designed as the main controller through maximizing the low-frequency gain with linear constraints from the system gain margin, phase margin and crossover frequency. Furthermore, a dynamics inversion based feedforward compensator and a disturbance observer are deliberately

designed to work with the PID to improve the dynamic response as well as to compensate for the system uncertainties.

With the optimized FTS, experimental test on the prototype suggests that a natural frequency of 3215 Hz and a stroke of 18 μm are practically obtained. With the closed-loop system, the maximum tracking error is observed to be about $\pm 1.5\%$ of the desired motion span when tracking a 100 Hz harmonic signal, which is only about 48.6% of the closed-loop system without adopting the disturbance observer. Moreover, a closed-loop bandwidth of about 1730 Hz is achieved from the frequency response function of the control system.

Practical turning using the developed FTS is performed on an ultra-precision machine tool to generate two typical micro-structured surfaces. The maximum tracking error with cutting force disturbances is examined to be less than $\pm 1.4\%$ of the motion span, and the feature dimensions of the generated micro-structured surfaces exhibit a good accordance with the desired surface, well demonstrating the effectiveness of the developed FTS for the generation of micro-structured surfaces.

REFERENCES

[1] E. Kouno and P. McKeown, "A fast response piezoelectric actuator for servo correction of systematic errors in precision machining," *CIRP Annals-Manufacturing Technology*, vol. 33, no. 1, pp. 369–372, 1984.

[2] M. Chen and C. Yang, "Dynamic compensation technology of the spindle error motion of a precision lathe," *Precision Engineering*, vol. 11, no. 3, pp. 135–138, 1989.

[3] W.-H. Zhu, M. B. Jun, and Y. Altintas, "A fast tool servo design for precision turning of shafts on conventional cnc lathes," *International Journal of Machine Tools and Manufacture*, vol. 41, no. 7, pp. 953–965, 2001.

[4] D. Wu and K. Chen, "Design and analysis of precision active disturbance rejection control for noncircular turning process," *IEEE Trans. Industrial Electronics*, vol. 56, no. 7, pp. 2746–2753, 2009.

[5] T. A. Dow, M. H. Miller, and P. J. Falter, "Application of a fast tool servo for diamond turning of nonrotationally symmetric surfaces," *Precision Engineering*, vol. 13, no. 4, pp. 243–250, 1991.

[6] H.-S. Kim, K.-I. Lee, K.-M. Lee, and Y.-B. Bang, "Fabrication of free-form surfaces using a long-stroke fast tool servo and corrective figuring with on-machine measurement," *International Journal of Machine Tools and Manufacture*, vol. 49, no. 12-13, pp. 991–997, 2009.

[7] Y.-L. Chen, S. Wang, Y. Shimizu, S. Ito, W. Gao, and B.-F. Ju, "An in-process measurement method for repair of defective microstructures by using a fast tool servo with a force sensor," *Precision Engineering*, vol. 39, pp. 134–142, 2015.

[8] S. Scheiding, Y. Y. Allen, A. Gebhardt, L. Li, S. Risse, R. Eberhardt, and A. Tünnermann, "Freeform manufacturing of a microoptical lens array on a steep curved substrate by use of a voice coil fast tool servo," *Optics express*, vol. 19, no. 24, pp. 23 938–23 951, 2011.

[9] A. Meier, "Diamond turning of diffractive microstructures," *Precision Engineering*, vol. 42, pp. 253–260, 2015.

[10] E. Brinksmeier, O. Riemer, R. Gläbe, B. Lünemann, C. Kopylow, C. Dankwart, and A. Meier, "Submicron functional surfaces generated by diamond machining," *CIRP annals*, vol. 59, no. 1, pp. 535–538, 2010.

[11] X.-D. Lu and D. L. Trumper, "Ultrafast tool servos for diamond turning," *CIRP Annals-Manufacturing Technology*, vol. 54, no. 1, pp. 383–388, 2005.

[12] D. Wu, X. Xie, and S. Zhou, "Design of a normal stress electromagnetic fast linear actuator," *IEEE Transactions on Magnetics*, vol. 46, no. 4, pp. 1007–1014, 2010.

[13] D. Wu and K. Chen, "Chatter suppression in fast tool servo-assisted turning by spindle speed variation," *International Journal of Machine Tools and Manufacture*, vol. 50, no. 12, pp. 1038–1047, 2010.

[14] H. Wang and S. Yang, "Design and control of a fast tool servo used in noncircular piston turning process," *Mechanical Systems and Signal Processing*, vol. 36, no. 1, pp. 87–94, 2013.

[15] H. Ma, D. Hu, and K. Zhang, "A fast tool feeding mechanism using piezoelectric actuators in noncircular turning," *The International Journal of Advanced Manufacturing Technology*, vol. 27, no. 3-4, pp. 254–259, 2005.

[16] A. Woronko, J. Huang, and Y. Altintas, "Piezoelectric tool actuator for precision machining on conventional cnc turning centers," *Precision Engineering*, vol. 27, no. 4, pp. 335–345, 2003.

[17] G. Sze-Wei, L. Han-Seok, M. Rahman, and F. Watt, "A fine tool servo system for global position error compensation for a miniature ultra-precision lathe," *International Journal of Machine Tools and Manufacture*, vol. 47, no. 7-8, pp. 1302–1310, 2007.

[18] W. Zhu, X. Yang, F. Duan, Z. Zhu, and B. Ju, "Design and adaptive terminal sliding mode control of a fast tool servo system for diamond machining of freeform surfaces," *IEEE Transactions on Industrial Electronics*, vol. 66, no. 6, pp. 4912–4922, 2019.

[19] Y. Yang, S. Chen, D. Huo, and K. Cheng, "Performance analysis and optimal design of fast tool servo used for machining microstructured surfaces," *Proceedings of the Institution of Mechanical Engineers, Part C: Journal of Mechanical Engineering Science*, vol. 222, no. 8, pp. 1541–1546, 2008.

[20] Z. Zhu, X. Zhou, Q. Liu, and S. Zhao, "Multi-objective optimum design of fast tool servo based on improved differential evolution algorithm," *Journal of mechanical science and technology*, vol. 25, no. 12, pp. 3141–3149, 2011.

[21] L. Zhang, "Compliant mechanisms design with fatigue strength control: a computational framework," Ph.D. dissertation, University of Saskatchewan, 2013.

[22] Y. Li and Q. Xu, "Adaptive sliding mode control with perturbation estimation and pid sliding surface for motion tracking of a piezo-driven micromanipulator," *IEEE Transactions on control systems technology*, vol. 18, no. 4, pp. 798–810, 2009.

[23] G.-Y. Gu, L.-M. Zhu, C.-Y. Su, H. Ding, and S. Fatikow, "Modeling and control of piezo-actuated nanopositioning stages: A survey," *IEEE Transactions on Automation Science and Engineering*, vol. 13, no. 1, pp. 313–332, 2014.

[24] A. Safa, R. Y. Abdolmalaki, and H. C. Nejad, "Precise position tracking control with an improved transient performance for a linear piezoelectric ceramic motor," *IEEE Transactions on Industrial Electronics*, vol. 66, no. 4, pp. 3008–3018, 2018.

[25] X. Chen, C.-Y. Su, Z. Li, and F. Yang, "Design of implementable adaptive control for micro/nano positioning system driven by piezoelectric actuator," *IEEE Transactions on Industrial Electronics*, vol. 63, no. 10, pp. 6471–6481, 2016.

[26] A. A. Dastjerdi, B. M. Vinagre, Y. Chen, and S. H. HosseinNia, "Linear fractional order controllers; a survey in the frequency domain," *Annual Reviews in Control*, vol. 47, pp. 51 – 70, 2019.

[27] D. P. Yu, G. S. Hong, and Y. San Wong, "Profile error compensation in fast tool servo diamond turning of micro-structured surfaces," *International Journal of Machine Tools and Manufacture*, vol. 52, no. 1, pp. 13–23, 2012.

[28] X. Yang, H. Liu, J. Xiao, W. Zhu, Q. Liu, G. Gong, and T. Huang, "Continuous friction feedforward sliding mode controller for a trimule hybrid robot," *IEEE/ASME Transactions on Mechatronics*, vol. 23, no. 4, pp. 1673–1683, 2018.

[29] M. Crudele and T. R. Kurfess, "Implementation of a fast tool servo with repetitive control for diamond turning," *Mechatronics*, vol. 13, no. 3, pp. 243–257, 2003.

[30] M. F. Byl, S. J. Ludwick, and D. L. Trumper, "A loop shaping perspective for tuning controllers with adaptive feedforward cancellation," *Precision Engineering*, vol. 29, no. 1, pp. 27–40, 2005.

[31] D. Wu and K. Chen, "Frequency-domain analysis of nonlinear active disturbance rejection control via the describing function method," *IEEE Transactions on Industrial Electronics*, vol. 60, no. 9, pp. 3906–3914, 2013.

[32] J. Yao and W. Deng, "Active disturbance rejection adaptive control of hydraulic servo systems," *IEEE Transactions on Industrial Electronics*, vol. 64, no. 10, pp. 8023–8032, 2017.

[33] W.-L. Zhu, Z. Zhu, Y. Shi, X. Wang, K. Guan, and B.-F. Ju, "Design, modeling, analysis and testing of a novel piezo-actuated xy compliant mechanism for large workspace nano-positioning," *Smart Materials and Structures*, vol. 25, no. 11, p. 115033, 2016.

[34] W.-L. Zhu, Z. Zhu, P. Guo, and B.-F. Ju, "A novel hybrid actuation mechanism based xy nanopositioning stage with totally decoupled kinematics," *Mechanical Systems and Signal Processing*, vol. 99, pp. 747–759, 2018.

[35] Z. Zhu, S. To, W.-L. Zhu, Y. Li, and P. Huang, "Optimum design of a piezo-actuated triaxial compliant mechanism for nanocutting," *IEEE Transaction on Industrial Electronics*, vol. 65, no. 8, pp. 6362–6371, 2018.

[36] K. Cheng, *Machining dynamics: fundamentals, applications and practices*. Springer Science & Business Media, 2008.

[37] C. Kai and D. Huo, *Micro-cutting: fundamentals and applications*. John Wiley & Sons, 2013.

[38] Z. Zhu, S. To, W.-L. Zhu, P. Huang, and X. Zhou, "Cutting forces in fast-/slow tool servo diamond turning of micro-structured surfaces," *International Journal of Machine Tools and Manufacture*, vol. 136, pp. 62–75, 2019.

[39] H. Li, R. Ibrahim, and K. Cheng, "Design and principles of an innovative compliant fast tool servo for precision engineering," *Mechanical Sciences*, vol. 2, no. 2, pp. 139–146, 2011.

[40] J. Li, H. Tang, Z. Wu, H. Li, G. Zhang, X. Chen, J. Gao, Y. Xu, and Y. He, "A stable autoregressive moving average hysteresis model in flexure fast tool servo control," *IEEE Transactions on Automation Science and Engineering*, 2019.

[41] J. Yi, S. Chang, and Y. Shen, "Disturbance-observer-based hysteresis compensation for piezoelectric actuators," *IEEE/ASME transactions on mechatronics*, vol. 14, no. 4, pp. 456–464, 2009.

[42] Ł. Ryba, A. Voda, and G. Besancon, "An lqg/ltr approach towards piezoactuator vibration reduction with observer-based hysteresis compensation," *IFAC Proceedings Volumes*, vol. 47, no. 3, pp. 5623–5628, 2014.

[43] M. Sadeghpour, V. de Oliveira, and A. Karimi, "A toolbox for robust pid controller tuning using convex optimization," *IFAC Proceedings*, vol. 45, no. 3, pp. 158 – 163, 2012.

[44] Y. Wu and Y. Ye, "Internal model-based disturbance observer with application to cvcf pwm inverter," *IEEE Transactions on Industrial Electronics*, vol. 65, no. 7, pp. 5743–5753, 2018.

[45] Y. Joo, G. Park, J. Back, and H. Shim, "Embedding internal model in disturbance observer with robust stability," *IEEE Transactions on Automatic Control*, vol. 61, no. 10, pp. 3128–3133, 2016.

[46] H. Shim and N. H. Jo, "An almost necessary and sufficient condition for robust stability of closed-loop systems with disturbance observer," *Automatica*, vol. 45, no. 1, pp. 296–299, 2009.